Corrosion Science 270 (2026) 113956

Contents lists available at ScienceDirect

Corrosion Science

journal homepage: www.elsevier.com/locate/corsci

High temperature oxidation of magnetron sputtered Y_2O_3 doped silicon bond coats for SiC/SiC CMCs

Ronja Anton [a,*], Vito Leisner [a], Philipp Watermeyer [b], Uwe Schulz [a]

[a] German Aerospace Center (DLR), Institute for Frontier Materials on Earth and in Space, Cologne 51147, Germany
[b] DLR, now at Max Planck Institute for Sustainable Materials, Düsseldorf 40237, Germany

ARTICLE INFO

Keywords:
Environmental barrier coating
Ceramic matrix composites
Physical vapour deposition
Silicon
Yttria
Bond coat

ABSTRACT

Silicon carbide (SiC) ceramic matrix composites (CMCs) are increasingly used in the high-temperature sections of turbine engines, requiring robust environmental barrier coating (EBC) systems to withstand extreme conditions. A silicon-based bond coat typically serves as the interface between the CMC and the EBC, although limitations remain for its long-term oxidation resistance and mechanical stability. In this study, yttria (Y_2O_3) doped silicon bond coats deposited by magnetron sputtering on monolithic SiC were investigated to improve these properties. Two compositions, 13 mol% and 25 mol% of $YO_{1.5}$ in silicon, were synthesized, yielding X-ray amorphous, homogeneous, and columnar structures. Furnace cycling tests were performed up to 1000 cycles at 1250 °C to evaluate the high temperature oxidation behavior of the coatings. Microstructural evolution and phase transformations were analyzed using scanning electron microscopy (SEM), focused ion beam (FIB), transmission electron microscopy (TEM), and X-ray diffraction (XRD). Upon thermal exposure, the films crystallized and during oxidation they form a thermally grown oxide (TGO) layer. The low-doped Y_2O_3 bond coat exhibited improved oxidation resistance, while the high-doped Y_2O_3 bond coat exhibited rapid pathways for oxygen due to the formation of yttrium disilicate ($Y_2Si_2O_7$), which induced pores and promoted inhomogeneous distribution of the Y_2O_3 phases. The study concludes that optimized Y_2O_3 doping can enhance oxidation resistance in Si based bond coat for CMC applications, with low Y_2O_3 content showing superior performance.

1. Introduction

Silicon carbide (SiC) ceramic matrix composites (CMCs) are increasingly utilized in high-temperature sections of turbine engines, notably as turbine shrouds. They are also promising candidates for replacing Ni-based superalloys in turbine blades due to their lower density, which is approximately one-third of that of Ni-based superalloys, thereby potentially increasing the thrust-to-weight ratio and enhancing aircraft efficiency. However, due to the severe oxidative environment of turbine engines, these CMCs require robust environmental barrier coating (EBC) systems. A silicon-based bond coat is typically used to provide oxidation protection, followed by an EBC layer to shield the CMC from water vapor corrosion [1–4]. Silicon bond coats are commonly applied due to silicon's ability to form a slow-growing SiO_2 layer. However, SiO_2 crystallizes into cristobalite, which undergoes phase transformations associated with significant thermal expansion mismatches, generating stresses that can cause cracking in the coating. Cristobalite has two polymorphs and transitions between its high and low temperature phases with a coefficient of thermal expansion (CTE) difference of about $7.2 \cdot 10^{-6}\ K^{-1}$ and a volume change of about 2.8%. The transition leads to stresses which are followed by mud cracking, especially in an increasing thermally grown oxide (TGO) layer [5–8]. In addition, Si only provides a low fractional toughness of about 0.8–0.9 MPa $m^{1/2}$, which can ultimately lead to delamination of the coating itself [9,10]. Thus, the long-term durability of pure silicon coatings is limited.

To address these challenges, several studies have investigated doping silicon bond coats with various oxides to enhance their oxidation resistance and mechanical stability. Several studies already investigated silicon bond coat using HfO_2 particles [11–21]. Most of the coatings are produced by atmospheric plasma spraying (APS) and are tested against oxidation at temperatures above 1200 °C. Bakan et al. examined the phase composition and microstructure of HfO_2-doped Si coatings, finding that after 100 h at 1300 °C, SiO_2 significantly increased while HfO_2 was largely consumed, forming $HfSiO_4$. The phase transformations in SiO_2 and the formation of $HfSiO_4$ contributed to coating cracking

* Corresponding author.
E-mail address: ronja.anton@dlr.de (R. Anton).

https://doi.org/10.1016/j.corsci.2026.113956
Received 13 March 2026; Received in revised form 15 May 2026; Accepted 16 May 2026
Available online 29 May 2026
0010-938X/© 2026 The Author(s). Published by Elsevier Ltd. This is an open access article under the CC BY license (http://creativecommons.org/licenses/by/4.0/).

during cyclic oxidation [14]. Chen also explored HfO_2 doping in Si coatings under steam oxidation and observed that $HfSiO_4$ formed at the SiO_2/HfO_2 interface, improving crack resistance through micro-crack deflection and pinning [19]. Deijkers further investigated a duplex bond coat approach, demonstrating that a two-layer Si + HfO_2 bond coat reduced the TGO layer thickness during steam cycling up to 1316 °C, delaying TGO cracking and delamination [12]. Ding also tested a multi-layered EBC system with a Si-HfO_2 bond layer, finding that the configuration effectively suppressed TGO growth at high temperatures. However, when the HfO_2 content exceeded 70 wt%, thermal mismatch led to interface peeling [17]. Additionally, Xiao tackled compositional challenges in Si-HfO_2 coatings due to differences in melting points and density, successfully producing a uniform coating through freeze drying. The study showed that uniformly distributed particles within the bond coat could improve durability and minimize crack initiation [21]. Lui's micromechanical analysis on HfO_2-Si composite coatings demonstrated improved resistance to crack propagation through the dispersed $HfSiO_4$ particles. However, excessive volume expansion from particle ripening led to interface separation over time [13]. Li found that Si-HfO_2 coatings with higher silicon content provided better thermal shock resistance, while Zhang observed that higher $HfSiO_4$ content in SiO_2-HfO_2 coatings improved stability up to 1475 °C [16,18]. In our previous study, we investigated magnetron sputtered coatings with a 36 mol% and 60 mol% HfO_2 content compared to a pure silicon coating at 1250 °C. Hafnia and the later formed hafnon increased the long-term stability of the coating. The low-doped silicon bond coat showed the best performance overall [11].

Ytterbium oxide (Yb_2O_3) has also shown promising results as a dopant in silicon bond coats to improve the oxidation resistance and mechanical properties of CMCs. Mao et al. showed that a Yb_2O_3 doped Si bond coat deposited by vacuum plasma spraying formed $Yb_2Si_2O_7$, thereby reducing the vertical cracks in the TGO and interfacial cracks, resulting in better bonding performance of the TGO layer [22]. Fan et al. investigated three different compositions of Yb_2O_3 doped Si bond coat within a full EBC system. The vacuum plasma sprayed coatings showed that the addition of about 10 vol% Yb_2O_3 improved the structural stability and reduced the cracking of the TGO by forming $Yb_2Si_2O_7$ during prolonged oxidation [23].

The primary aim of this study is to improve the properties of silicon bond coat by Y_2O_3 dopant using PVD technology. Y_2O_3 was chosen for its ability to form yttrium silicates (Y_2SiO_5 and $Y_2Si_2O_7$) when combined with SiO_2, which have favorable properties for EBCs. The disilicate, $Y_2Si_2O_7$, is particularly advantageous because its CTE is close to that of SiC, minimizing thermal stresses. Both silicates have low Young's modulus, low water vapor set rates and high erosion resistance [24–30]. While the low fracture toughness of silicon contributes to coating delamination, the primary design objective of Y_2O_3 doping in this study is to suppress the phase transformation stress associated with cristobalite formation by promoting the formation of thermally compatible β-$Y_2Si_2O_7$. Therefore, the current study investigates the potential of yttria doped silicon bond coats for improved protection of SiC/SiC CMCs in extreme environments and as future bond coats for EBCs.

2. Experimental

The model substrate material used was monolithic α-SiC (Hexology SA, CoorsTek GmbH, Mönchengladbach, Germany) with a roughness of $R_a = 0.3$ μm, which provides a relatively rough surface for PVD coatings and a chemistry similar to that of the SiC/SiC CMCs. The sample dimensions were 10 mm · 10 mm · 4 mm. The coatings were deposited using a batch magnetron sputtering system (Z 400, Systec SVS vacuum coatings, Karlstadt, Germany). Prior to coating deposition, one side of the sample was subjected to Ar^+ ion etching to clean and activate the sample surface. Dense polycrystalline targets of Si and Y_2O_3 with a diameter of 100 mm were used as targets, placed face to face. DC/RF co-sputtering was performed at different target powers to obtain coatings with two different stoichiometries. The power applied to the Y_2O_3 target was adjusted to achieve two distinct target compositions, referred to as low-doped and high-doped Y_2O_3. For the low-doped variant, the power settings were 800 W for Si and 230 W for Y_2O_3, while the high-doped version used 400 W for Si and 230 W for Y_2O_3. Deposition was carried out at a total pressure of 0.45 Pa in an argon atmosphere with a constant flow rate of 25 sccm. The substrate temperature naturally rose to approximately 130 °C during the process, without the need for external heating. To ensure uniform coating, the samples were rotated at 12 rpm throughout deposition, resulting in a deposition rate of about 2 μm/h. The coated samples were subjected to a furnace cycle test in laboratory air. A vertical tube furnace was heated to 1250 °C, and the samples were directly inserted into the hot zone. Each sample underwent a 60 min annealing cycle at this temperature, which included a heating phase at a rate of approximately 70 °C/min, followed by a 10 min active cooling phase in flowing air, bringing the temperature down to near room temperature. The thermocouple mounted on the sample holder recorded a heating rate of approximately 70 °C/min during insertion into the furnace. By tracking the weight change after certain cycles, the oxidation kinetics could be analysed. One sample of each type was not tested in order to examine the as-coated condition after deposition.

All samples were examined using a variety of analytical instruments. X-ray diffraction was performed in a Siemens D5000 using Cu-Kα radiation (EVA/Topas 4.2 software package, Bruker AXS, Karlsruhe, Germany). In order to understand the crystallization process of the coating, high-temperature XRD (HT-XRD) was carried out with a heating furnace chamber (HTK 1200 N, Anton Paar, Graz, Austria) within a Bruker D8 Advance. The temperature profil was chosen to mimic the crystallization during testing, therefore a high rate of 40 /min was set. The temperature limit of the chamber is 1200 °C, the test was set for 10 h at this temperature. Scanning electron microscopy (SEM) using a DMS Ultra 55 (Carl Zeiss NTS, Wetzlar, Germany) with an acceleration voltage of 5 kV was used for microstructural analysis. Energy dispersive X-ray spectroscopy (EDS) (Aztec, Oxford Instruments, Abingdon, UK) was performed at 15 kV to determine the elemental distribution. To determine the polymorphic phases of $Y_2Si_2O_7$, transmission electron microscopy (TEM) (Tecnai F30 TEM/STEM FEI Philips, Netherlands) was performed on the high-doped Y_2O_3 bond coat after 500 h of thermocycle oxidation. The lamella was prepared by a focused ion beam (FIB) (Dual Beam FEI Helios, FEI Philips, Netherlands).

3. Results

3.1. Microstructure

3.1.1. Low-doped Y_2O_3 silicon bond coat

The morphology of the coatings with 13 mol% $YO_{1.5}$ shows a typical PVD coating with a columnar structure. The gaps between the columns are very small, giving the coating a very dense appearance. No pores are visible. The thickness of the coating is approximately 8.5 μm. The top view shows a typical cauliflower appearance.

After 10 h of testing at 1250 °C, the bond coat shows bright precipitates in a silicon matrix; the bright precipitates can be identified by EDS as rich in yttrium oxide, they are nanometer sized and homogeneously distributed throughout the coating. Pores can also be seen which are partially filled with Al_2O_3, originating from the polishing agent. The coating formed a dense, thermally grown oxide layer of SiO_2, which also contained small precipitates rich in yttrium oxide. The total layer thickness including the TGO increased to 11.8 μm. The coating showed very good adhesion to the substrate. After a test period of 100 h, the yttria-rich precipitates and the pores became increasingly interconnected. The increased size allowed the precipitates to be identified as yttrium disilicate, $Y_2Si_2O_7$. The TGO layer also increased in thickness and was clearly identified by a horizontal boundary, marked by a dotted line in Fig. 2. The Y-rich precipitates are much smaller in the outer TGO zone compared to their size in the silicon-containing region underneath.

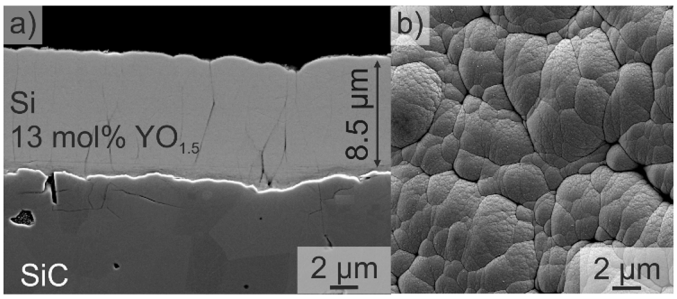


Fig. 1. Micrographs of the low-doped Y_2O_3 silicon bond coat in the as-coated state; a) cross-section; b) top view.

Vertical cracks in the oxide layer are clearly visible. The coatings shown reach a total thickness of approximately 12.6 µm. The longest test period of 1000 h shows a significant difference in the $Y_2Si_2O_7$ particle size and pore size. The TGO thickness increased and the vertical cracks in the oxide layer, which can spread horizontally at the interface between the TGO and the Si layer, are also clearly visible. Internal oxidation of silicon is clearly visible around the yttria precipitates within the bond coat. The total thickness after 1000 h is about 14.7 µm. The top view of the sample shows the crack formation pattern. However, these do not lead to any large-scale delamination of the coating.

3.1.2. *High-doped Y_2O_3 silicon bond coat*

The microstructure of the high yttria doped coating after deposition is shown in Fig. 3. The coating consists of 25 mol% $YO_{1.5}$ and silicon and has a thickness of 10.4 µm. The top view of the coating shows the cauliflower growth.

After 10 h of thermocycle oxidation, the coating has a thickness of about 13 µm, as shown in Fig. 4. Pores and precipitates can be seen distributed throughout the coating. As in the low-doped Y_2O_3 layer, these can be identified as $Y_2Si_2O_7$. The pores are partially filled with polishing agent particles. A thin TGO consisting of SiO_2 and small precipitates can be seen, marked by a doted line in Fig. 4 (left and middle). After 100 h, the TGO increases significantly in thickness and a few cracks can be seen inside. In addition, internal SiO_2 phases form around the $Y_2Si_2O_7$ precipitates. The precipitates grow together as well as the pores. The thickness of the layer is about 12.2 µm after 100 h. The top layer above the dotted lines consists of finer Y-rich precipitates. After 1000 h of thermocycle oxidation, the proportion of the SiO_2 phase is greater than that of the silicon phase in the coating. The $Y_2Si_2O_7$ precipitates (light coloured) are surrounded by oxidized silicon (dark grey), while no precipitates are seen in the non-oxidized silicon. The total thickness of the layer is approximately 16 µm. Cracks in the top view show that the SiO_2 phase is also damaged by the thermocycle loading. Minor chipping can also be seen. A continuous (silicon-)oxide layer on the surface is not visible.

3.2. *Phase analysis*

To understand the crystallization process in the initial stage and investigate the speed of yttrium disilicate formation, HT-XRD was performed. Due to the heating chamber's limitations, the maximum temperature was 1200 °C. The measurement was performed similar to the oxidation tests; therefore, a fast heating rate of 40°/min was chosen. The test lasted 10 h at 1200 °C, followed by cooling down again. During heating, crystallization of the coating begins at approximately 780 °C and continues up to around 1030 °C. Since the heating measurement was programmed to be very fast, small peaks were difficult to detect. This is why only the silicon peak could be seen during crystallization. In Fig. 5 the HT-XRD measurement obtained in the as-coated state, after 1 h at 1200 °C, after 10 h at 1200 °C, and after cooling to 30 °C. No distinct phase transformations are observed after crystallization up to 1 h at 1200 °C; however, SiO_2 formation becomes evident between 1 h and 10 h at 1200 °C. No additional phase changes are detected upon cooling.

At room temperature conditions, both coatings were studied by XRD analysis from the as-coated state up to the 1000 h thermocycle test, see Fig. 6. Immediately after deposition, in the as-coated state, both coatings are X-ray amorphous with only SiC peaks present from the substrate material. After 10 h of testing, both coatings show the formation of SiO_2, silicon and various polymorphes of $Y_2Si_2O_7$. In the low-doped Y_2O_3 coating scans, α,β, and y-$Y_2Si_2O_7$ can be identified. SiO_2 is identified as α-cristobalite in all scans shown in Fig. 6. The low temperature phase y-$Y_2Si_2O_7$ is found only in the 10 h sample. The α-$Y_2Si_2O_7$ phases show reduced intensities with increasing testing time, while β-$Y_2Si_2O_7$ is present from 500 h on. In the high-doped Y_2O_3 coating, two different polymorphes of yttrium disilicate are found in the samples. These are α- and β-$Y_2Si_2O_7$. The α-$Y_2Si_2O_7$ can only be detected by very few peaks, while β-$Y_2Si_2O_7$ increases in peak number and intensity from 10 h to 1000 h. The SiO_2 signal increases with longer exposure time in the thermocycle experiment. The low-doped Y_2O_3 silicon coatings show less formation of $Y_2Si_2O_7$, while the high-doped Y_2O_3 silicon coatings show larger peaks for this phase. The SiO_2 peak is very significant in the high-doped Y_2O_3 coating after 1000 h, while the silicon signal decreases, which is consistent with the results from the SEM micrographs in Fig. 4. In contrast, the low-doped Y_2O_3 coatings also show an increase in SiO_2 formation, but the silicon signal, although decreasing, remains significant.

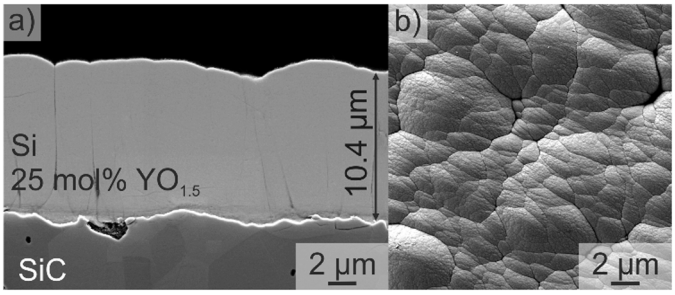


Fig. 3. Micrographs of the high-doped Y_2O_3 silicon bond coat in the as-coated state; a) cross-section; b) top view.

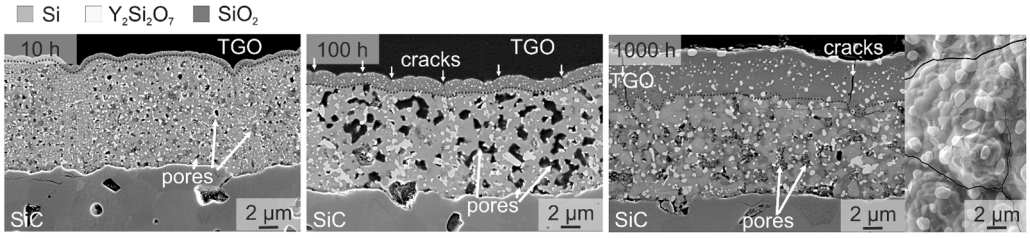


Fig. 2. Micrograph of the low-doped Y_2O_3 silicon bond coat after 10 h, 100 h and 1000 h (and top view) of thermocycle testing at 1250 °C. The dotted line separates the TGO from the coating.

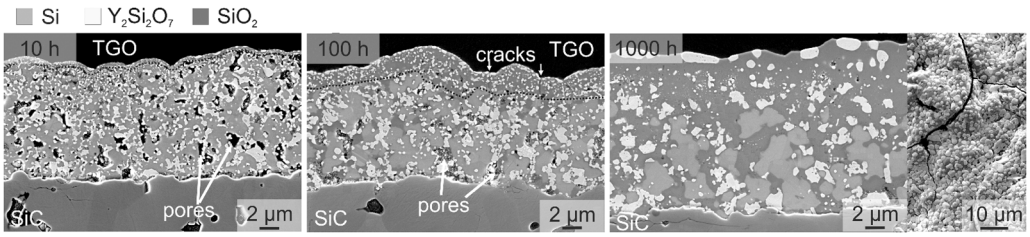


Fig. 4. Micrograph of the high-doped Y_2O_3 silicon bond coat after 10 h, 100 h and 1000 h (and top view) of thermocycle testing at 1250 °C. The dotted line separates the TGO from the coating.

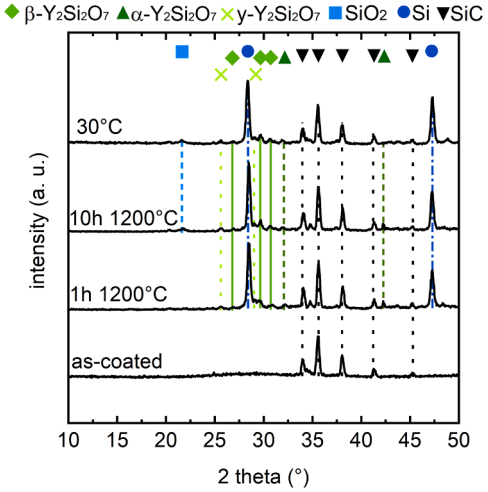


Fig. 5. HT-XRD scan of the low-doped Y_2O_3 bond coat for 10 h at 1200 °C.

In order to closely investigate the different polymorphes of $Y_2Si_2O_7$, a FIB lamella was produced from the high-doped Y_2O_3 coating after a testing time of 500 h. This sample was selected to have sufficiently large precipitates and both polymorphic phases within the coating. Two areas of the lamella, near the substrate and near the surface, were thinned to be transparent to the electron beam, see Fig. 7. Three grains were selected for single crystal diffraction to determine their phases. EDS and XRD analyses, shown previously, already proofed the formation of $Y_2Si_2O_7$. However, these analytical methods could not provide information about which polymorphes of the yttrium disilicate occur in which regions of the coating. TEM-EDS measurements show that the light colored phases can be assigned to a yttrium disilicate phase. Grain 3 and grain 1 are precipitates closer to the substrate in the unoxidized silicon phase and grain 2 is further away from the substrate in the silicon oxide phase. Diffraction of the three grains yields the β-$Y_2Si_2O_7$ phase (PDF 00–038–0440) for grain 2 and grain 3. The first precipitate, grain 1, can be characterized as α-$Y_2Si_2O_7$ (PDF 00–038–0223).

3.3. Oxidation kinetics of the Y_2O_3 doped silicon bond coat

To evaluate the oxidation kinetics of the Y_2O_3 doped bond coats, the weight of the samples was measured throughout the thermocycle oxidation at 1250 °C up to 1000 h. In Fig. 8, the mass change per area is presented of the Y_2O_3 doped bond coats as well as bond coats represented in [11] for comparable reasons. The weight change was measured by using a microgram scale. Since the samples were coated only from one side, the amount of weight change observed for a bare SiC sample was subtracted from the data to achieve the pure weight changes induced by the coating. During the thermocyclic oxidation test, an increase in the sample weight is observed, which does not appear to reach a maximum value for both Y_2O_3 doped coatings. The Y_2O_3 doped coatings still show a gradient in their curves up to the last measured value after 1000 h. The high-doped Y_2O_3 bond coat shows the greatest increase in mass between two measuring points at 30 h and 40 h of thermocyclic oxidation. The right diagram in Fig. 8 shows the TGO thickness evolution over the testing time. Since the TGO thickness of the high-doped Y_2O_3 bond coat cannot be distinguished clearly, only the

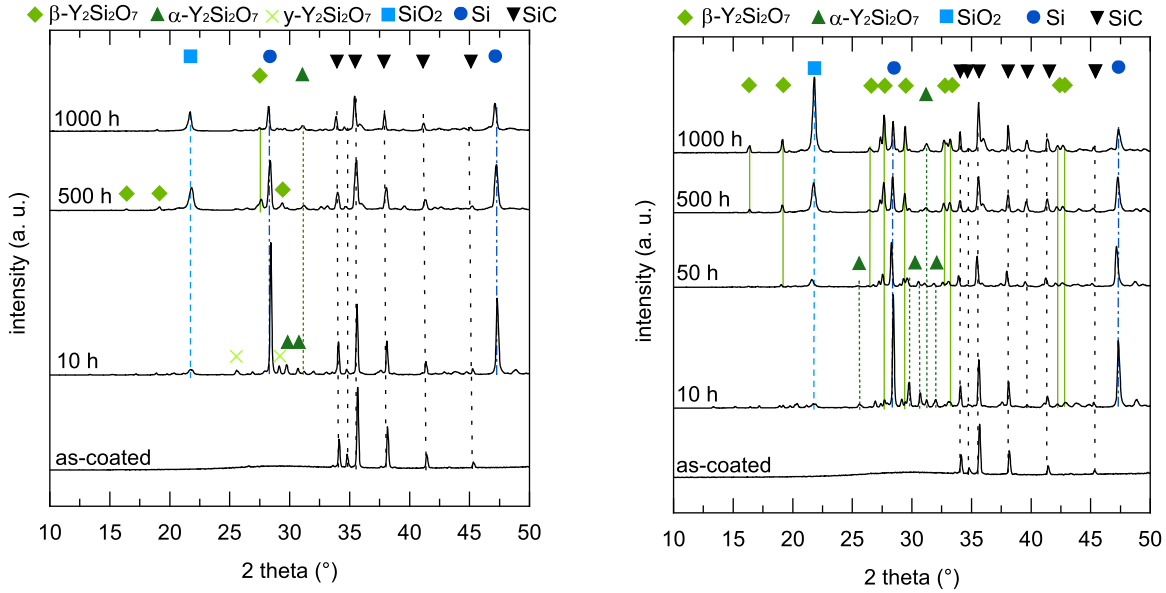


Fig. 6. XRD scan of the yttria-doped bond coat for different testing times at 1250 °C; left: low-doped Y_2O_3, 13 mol% $YO_{1.5}$; right: high-doped Y_2O_3, 25 mol% $YO_{1.5}$.

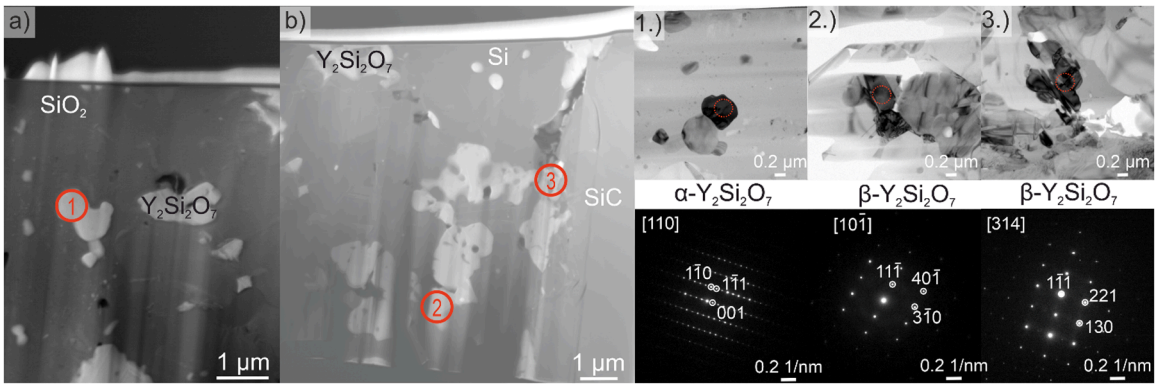


Fig. 7. FIB-lamella of the high-doped Y_2O_3 bond coat in TEM after 500 h of thermocycle testing at 1250 °C; a) HAADF image of surface near region; b) HAADF image of substrate near region; 1.–3.) bright field image and corresponding diffraction image.

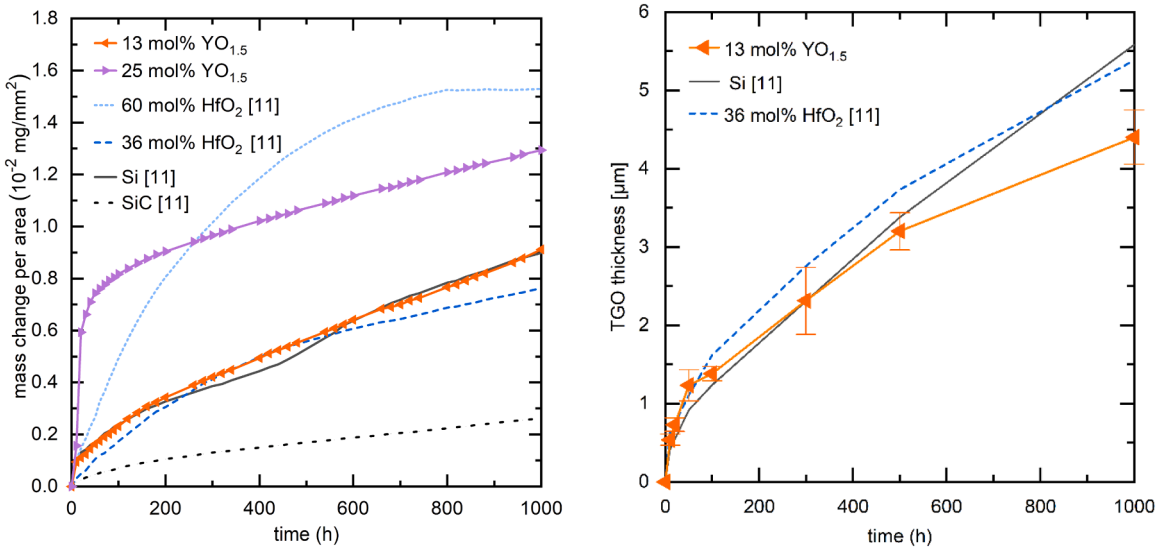


Fig. 8. Oxidation kinetics of the Y_2O_3 doped bond coats during thermocyclic oxidation at 1250 °C compared to date of pure silicon and HfO_2 doped bondcoats from [11]; left: mass change per area; right: TGO thickness development over time.

low-doped Y_2O_3 bond coat is shown.

The weight change values determined during the oxidation test were used to calculate the parabolic growth constant. For the low-doped Y_2O_3 bond coat samples, the growth constants can be determined over the entire period, as they are approximately linear. The constant of the high-doped Y_2O_3 bond coat is only permissible for the period of 40 h – 1000 h. The results are presented in Table 1.

4. Discussion

4.1. Influence of doping content on phase formation and microstructural evolution

In the as-coated state, magnetron-sputtered silicon bond coats doped with Y_2O_3 exhibit a fine distribution of Si, O, and Y atoms, along with vacancies throughout the coating. Inter-columnar gaps are visible in the top-view micrographs (Fig. 1 and Fig. 3). Such structural characteristics are inherent to the sputtering process and define the film's initial microstructural state [31].

Upon crystallization and oxidation testing in laboratory air at elevated temperatures, a series of reactions occurs driven by the thermodynamic affinities of the constituent elements. Yttrium, owing to its high affinity for oxygen, reacts preferentially with both oxygen already present in the as-deposited coating and oxygen supplied from the surrounding atmosphere to form crystalline Y_2O_3, while silicon crystallizes into a pure Si phase [32,33]. Inter-columnar gaps and vacancies provide fast pathways for external oxygen ingress, allowing oxygen to penetrate deeply into the coating. This process leads to progressive closure of the columnar structure through oxide formation. Similar behavior has been reported in earlier studies on silicon bond coats, where oxygen uptake through structural voids led to rapid oxidation and sealing-off effects [11,34–36].

The presence of Y_2O_3 enhances oxygen transport by providing fast diffusion pathways [37]. This increased local oxygen availability promotes preferential oxidation of silicon in the vicinity of Y_2O_3 particles, resulting in SiO_2 formation. The subsequently formed SiO_2 reacts with Y_2O_3 to produce $Y_2Si_2O_7$ disilicate. This reaction sequence is accompanied by coating thickening and the formation of porosity around the $Y_2Si_2O_7$ precipitates. The preferential formation of $Y_2Si_2O_7$ is

Table 1
Mass change after 1000 h of FCT and parabolic growth constant of the Y_2O_3 doped bond coat variants over the testing time.

Bond coat	Mass change after 1000 h of FCT (µg/mm²)	Growth constant (10^{-11} kg²/(m⁴s))
Si – 13 mol% $YO_{1.5}$	9.11	2.16 (0 – 1000 h FCT)
Si – 25 mol% $YO_{1.5}$	12.94	3.16 (40 – 1000 h FCT)

thermodynamically expected due to the high silicon content of the coating and the SiO_2–Y_2O_3 phase diagram favoring disilicate formation. The consequences of rapid oxygen transport through Y_2O_3 and, at later stages, through $Y_2Si_2O_7$ are evident in Fig. 4 after 100 h and more clearly after 1000 h of cyclic oxidation [38]. The silicon bond coat oxidizes preferentially around the $Y_2Si_2O_7$ precipitates which is comparable to the results shown by Mao et al. [22].

As shown in Fig. 2 and Fig. 4, the size and morphology of the $Y_2Si_2O_7$ precipitates depend strongly on the surrounding matrix. Within the TGO, the precipitates are small and predominantly round-shaped, whereas in the mostly unoxidized regions of the coating significantly larger precipitates are observed. Although Ostwald ripening is thermodynamically favored in both environments, reduced cation mobility in the SiO_2-rich matrix kinetically suppresses precipitate coarsening relative to the Si matrix [28,29,37,38].

XRD analyses (Fig. 5 and Fig. 6) identify cubic silicon and α-cristobalite as silicon-containing phases. The Y_2O_3 dopant transforms rapidly during or shortly after crystallization into $Y_2Si_2O_7$ precipitates. Three polymorphs of $Y_2Si_2O_7$ (β-, α-, and γ-phase) are detected. With decreasing Y_2O_3 content, the relative phase fractions change, while the phase assemblage remains identical. With prolonged oxidation, residual silicon is progressively converted into cristobalite.

As the test time increases, the β-phase, which is favorable in terms of CTE, increases at the expense of the α- and γ-phases. It is known from the literature that γ-$Y_2Si_2O_7$ transforms to β-$Y_2Si_2O_7$ at around 1050°C, while α-$Y_2Si_2O_7$, as the first high-temperature phase, transforms reversibly to β-$Y_2Si_2O_7$ at around 1225°C [39]. The α-phase exhibits a thermal expansion coefficient approximately twice that of the β-phase, which can induce significant thermomechanical stresses. Consequently, stabilization of β-$Y_2Si_2O_7$, owing to its closer thermal expansion match with both Si and SiO_2, becomes energetically favorable and leads to an increasing β-phase fraction with prolonged ageing. High cooling rates further favor the retention of β-$Y_2Si_2O_7$, as the reversible transformation back to α- or γ-$Y_2Si_2O_7$ is kinetically suppressed [40].

TEM analysis of the layer after 500 h of cyclic oxidation confirms the coexistence of α- and β-$Y_2Si_2O_7$ based on three grains analyzed (Fig. 7). Grains close to the substrate correspond to the β-phase, whereas grains farther from the substrate are identified as α-phase. Although the limited number of analyzed grains precludes generalization, local cooling conditions, mechanical stresses, and cristobalite transformation are likely to influence phase stability on a local scale.

4.2. *Influence of doping content on oxidation behaviour and performance*

In line with previous findings [11], oxidation of the pure silicon coating results in the formation of a distinct SiO_2 TGO surface layer. Silicon oxidation also occurs in the Y_2O_3-doped coatings. However, the oxidation morphology and kinetics differ markedly with dopant content. In the low-doped coating, a continuous and fully oxidized TGO layer becomes visible only after 1000 h of thermocyclic testing, while localized internal oxidation of silicon initiates after approximately 100 h. In contrast, in the higher-doped variant, the initially formed SiO_2 appears as a TGO layer, but after about 50 h of cyclic oxidation, silicon oxide phases grow rapidly within the coating. Consequently, a distinct TGO layer can no longer be identified beyond 50 h, indicating accelerated internal oxidation. After approximately 1000 h, the entire coating is converted into an oxide mixture. The initial columnar microstructure with inter-columnar voids, characteristic of PVD deposition, plays a dual role. It facilitates controlled oxygen ingress in the low-doped coating, enabling the formation of a stable, well-defined TGO layer, while in the high-doped coating, it accelerates internal oxidation through the $Y_2Si_2O_7$ precipitates, leading to rapid degradation.

The onset of thermocyclic ageing is governed by oxidation of silicon along the columnar grain structure, resulting in SiO_2 formation. The subsequently formed SiO_2 reacts rapidly with Y_2O_3 to produce $Y_2Si_2O_7$, leaving behind a porous microstructure (Fig. 2, Fig. 4 and Fig. 5). A lower Y_2O_3 content results in smaller and more isolated $Y_2Si_2O_7$ precipitates, whereas higher doping promotes the formation of coarser disilicate precipitates. The reaction between Y_2O_3 and SiO_2 forming $Y_2Si_2O_7$ proceeds rapidly and is nearly complete at around 1200 °C, which is shown in Fig. 5.

Initially, pores formed during this transformation are small but agglomerate via diffusion-controlled processes. In Si-rich regions, higher atomic mobility promotes pore migration and coalescence, whereas pore growth is kinetically constrained in SiO_2-rich regions. With continued oxidation, pores begin to close as SiO_2 grows. In the low-doped coating, slower TGO growth limits pore closure, leading to crack initiation after approximately 100 h. After 1000 h, only a small fraction of these cracks evolve into mud cracks, resulting in limited delamination.

In the high-doped coating, larger initial pore volumes form due to rapid $Y_2Si_2O_7$ formation and enhanced internal oxidation. Although accelerated SiO_2 growth eventually fills much of the porosity, the associated volume expansion and internal stress accumulation promote crack formation. Nevertheless, large-scale delamination is avoided due to stress accommodation by porosity and distributed silicate phases. In particular, a reduced density of vertical cracks within the oxidized upper layers and less TGO spallation are observed in the Y_2O_3-doped coatings compared to the pure silicon layer, with this effect being more pronounced for the higher Y_2O_3-doped variant.

Oxidation kinetics confirm these observations summarized in Table 1. The low-doped Y_2O_3 coating exhibits a parabolic growth coefficient of $2.16 \cdot 10^{-11}$ $kg^2/(m^4\ s)$, which is 1.46 times lower than that of the high-doped Y_2O_3 variant. SEM micrographs (Fig. 2) clearly show TGO development. Passive oxidation accompanied by weight gain dominates in both cases. In the low-doped Y_2O_3 coating, the fine $Y_2Si_2O_7$ precipitates limit internal oxidation, but the TGO alone does not fully prevent oxygen ingress. The high-doped Y_2O_3 coating, in contrast, shows a higher parabolic growth constant of $3.16 \cdot 10^{-11}$ $kg^2/(m^4\ s)$ (valid from 40 h to 1000 h) and lacks a well-defined, horizontal TGO interface (Fig. 4).

Among all tested coatings including previously published data, parabolic rate constants follow this trend: low-doped HfO_2 = low-doped Y_2O_3 = pure Si < high-doped Y_2O_3 < high-doped HfO_2, see Fig. 8. This indicates that an excessive oxide content embedded into silicon enhances oxygen diffusion, whereas moderate doping slows down oxidation comparable to pure silicon.

After 1000 h, TGO thickness ratios reflect these kinetics (Fig. 8). The 13 mol% $YO_{1.5}$ coating exhibits a TGO-to-total-thinkness ratio of ~30%, the low-doped HfO_2 coating ~38%, and pure silicon ~39%, whereas the 60 mol% HfO_2 coating is fully oxidized. The 25 mol% $YO_{1.5}$ coating shows oxide phases throughout its thickness, while residual silicon persists in the lower regions. This behavior arises from heterogeneous, transport-controlled reactions: oxygen diffuses efficiently through Y_2O_3/$Y_2Si_2O_7$ precipitates, while reduced cation mobility within silicate and SiO_2 phases kinetically isolates some silicon grains, preventing complete oxidation. Consequently, a distinct TGO thickness cannot be defined for this coating.

Overall, the results demonstrate that yttria additions strongly influence both phase evolution and oxidation behavior. Moderate Y_2O_3 doping (13 mol% $YO_{1.5}$) promotes the formation of the thermomechanically compatible β-$Y_2Si_2O_7$ phase, leading to improved oxidation resistance and coating stability. Excessive doping, however, accelerates internal oxidation due to increased oxygen diffusivity through Y_2O_3 and $Y_2Si_2O_7$, resulting in higher porosity and stress formation. Nevertheless, both doped coatings outperform the undoped silicon layer by maintaining adhesion, lowering vertical cracking in the TGO, and suppressing large-scale delamination during prolonged cyclic oxidation.

The oxidation behavior of Y_2O_3-doped silicon coatings observed in this work shows parallels and distinctions to other oxide-modified silicon bond coats, particularly those doped with HfO_2 [11–21] and Yb_2O_3 [22,23]. In all systems, improved oxidation resistance results from the

in-situ formation of thermochemically stable silicates ($HfSiO_4$, $Yb_2Si_2O_7$, and $Y_2Si_2O_7$), which initially act as oxygen transport pathways but subsequently stabilize the microstructure while SiO_2 is forming a continuous layer that reduces further oxidation at high temperature. The formation of the silicate consumes SiO_2 which is favorable to decrease the stresses during cristobalite transformation.

Overall, Y_2O_3-doped coatings combine features of both HfO_2- and Yb_2O_3-based systems: they form stable disilicates that initially enhance oxygen transport but ultimately stabilize the TGO and maintain adhesion. The low-doped Y_2O_3 coating therefore represents the optimal compromise between oxidation resistance and mechanical stability among the tested variants and is thus an excellent candidates as an bond coat for an EBC system.

5. Conclusions

Magnetron-sputtered silicon bond coats doped with different Y_2O_3 contents (13 and 25 mol% $YO_{1.5}$), were investigated to elucidate the influence of oxide additions on phase formation, microstructural evolution, and oxidation behaviour at 1250 °C. The following conclusions can be drawn:

1. Phase formation and transformation: In the as-coated state, both low- and high-doped coatings exhibit a fine columnar microstructure with inter-columnar voids characteristic of sputtered films. Upon oxidation, Y_2O_3 rapidly reacts with SiO_2 to form $Y_2Si_2O_7$. Three polymorphs (α-, β-, and γ-$Y_2Si_2O_7$) were detected, with the β-phase dominating after prolonged cyclic oxidation. The stabilization of β-$Y_2Si_2O_7$, owing to its favorable thermal expansion match with Si and SiO_2, minimizes thermal stresses and enhances structural compatibility during cycling.
2. Microstructural evolution: The conversion of Y_2O_3 to $Y_2Si_2O_7$ leads to transient porosity due to density differences between reactants and products. In the low-doped coating (13 mol% $YO_{1.5}$), slower oxidation kinetics allow gradual pore closure and maintain coating integrity. In contrast, the high-doped variant (25 mol% $YO_{1.5}$) exhibits faster internal oxidation and coalescence of oxide phases, resulting in a more porous structure and occasional localized cracking. Nevertheless, large-scale delamination was not observed in either doped coating.
3. Oxidation behaviour: Both coatings follow parabolic oxidation kinetics, with the low-doped variant showing the lower growth constant ($2.16 \cdot 10^{-11}$ kg^2 m^{-4} s^{-1}), indicating improved oxidation resistance. The higher Y_2O_3 content accelerates oxidation due to enhanced oxygen diffusivity through Y_2O_3 and $Y_2Si_2O_7$. The low-doped coating thus provides the most balanced combination of oxidation protection and mechanical stability.

In summary, moderate Y_2O_3 doping (≈ 13 mol% $YO_{1.5}$) offers the most effective strategy to enhance the oxidation resistance and structural stability of magnetron-sputtered silicon bond coats. The rapid formation and persistence of the β-$Y_2Si_2O_7$ phase ensure good thermal compatibility and mechanical integrity under long-term cyclic oxidation at 1250 °C.

CRediT authorship contribution statement

Ronja Anton: Writing – review & editing, Writing – original draft, Visualization, Methodology, Investigation, Formal analysis, Conceptualization. **Vito Leisner:** Writing – review & editing, Methodology, Conceptualization. **Philipp Watermeyer:** Writing – review & editing, Investigation. **Uwe Schulz:** Writing – review & editing, Supervision, Resources.

Declaration of Competing Interest

The authors declare that they have no known competing financial interests or personal relationships that could have appeared to influence the work reported in this paper.

Acknowledgments

For the technical support at the DLR – German Aerospace Center the authors thanks A. Handwerk.

Data Availability

Data will be made available on request.

References

[1] R.C. Robinson, J.L. Smialek, SiC recession caused by SiO2 scale volatility under combustion conditions: I, Experimental results and empirical model, J. Am. Ceram. Soc. 82 (7) (1999) 1817–1825, https://doi.org/10.1111/j.1151-2916.1999.tb02004.x.
[2] V. Leisner, A. Lange, P. Mechnich, U. Schulz, Magnetron Sputtered Y2SiO5 Environmental Barrier Coatings For SIC/SIC CMCS. Advances in High Temperature Ceramic Matrix Compo sites and Materials for Sustainable Development; Ceramic Transactions, Volume CCLXIII John Wiley & Sons, Inc, 2017, pp. 197–209, https://doi.org/10.1002/9781119407270.ch20, 9781119407270.
[3] H.E. Eaton, G.D. Linsey, Accelerated oxidation of SiC CMC's by water vapor and protection via environmental barrier coating approach, 14, J. Eur. Ceram. Soc. 22 (2002) 2741–2747, https://doi.org/10.1016/S0955-2219(02)00141-3.
[4] R.A. Golden, E.J. Opila, A method for assessing the volatility of oxides in high-temperature high-velocity water vapor, J. Eur. Ceram. Soc. 36 (5) (2016) 1135–1147, https://doi.org/10.1016/j.jeurceramsoc.2015.11.016.
[5] K.N. Lee, Environmental Barrier Coatings for SiCf/SiC, in: N.P. Bansal, J. Lamon (Eds.), Ceramic Matrix Composites, John Wiley & Sons, 2014, pp. 430–451, https://doi.org/10.1002/9781118832998.ch15, 9781118832998978111823116 6.
[6] Y. Okada, Y. Tokumaru, Precise determination of lattice parameter and thermal expansion coefficient of silicon between 300 and 1500 K, J. Appl. Phys. 56 (2) (1984) 314–320, https://doi.org/10.1063/1.333965.
[7] B.T. Richards, S. Sehr, F. de Franqueville, M.R. Begley, H.N.G. Wadley, Fracture mechanisms of ytterbium monosilicate environmental barrier coatings during cyclic thermal exposure, Acta Mater. 103 (2016) 448–460, https://doi.org/10.1016/j.actamat.2015.10.019.
[8] H. Salmang, H. Scholze, and R. Telle, in: Keramik, 3540109870, Springer, 1982.
[9] W.D. Sylwestrowicz, Mechanical properties of single crystals of silicon, Philos. Mag. 7 (83) (1962) 1825–1845, https://doi.org/10.1080/14786436208213849.
[10] D. Zhu, Development and performance evaluations of HfO2-Si and rare earth-Si based environmental barrier coating systems for SiC/SiC ceramic matrix composites, Int. Conf. Metall. Coat. Thin Films San. Diego 41 (2014).
[11] R. Anton, V. Leisner, P. Watermeyer, M. Engstler, U. Schulz, Hafnia-doped silicon bond coats manufactured by PVD for SiC/SiC CMCs, Acta Mater. 183 (2020) 471–483, https://doi.org/10.1016/j.actamat.2019.10.050.
[12] J.A. Deijkers, H.N.G. Wadley, A duplex bond coat approach to environmental barrier coating systems, Acta Mater. 217 (2021) 117167, https://doi.org/10.1016/j.actamat.2021.117167.
[13] R. Liu, W. Liang, Q. Miao, H. Zhao, S. Zuo, W. Chen, X. Tao, Micromechanical analysis and theoretical predictions towards thermal shock resistance of HfO2-Si environmental barrier coatings, Compos. Part B Eng. 226 (2021) 109334, https://doi.org/10.1016/j.compositesb.2021.109334.
[14] E. Bakan, Y.J. Sohn, R. Vaßen, Microstructure and phase composition evolution of silicon-hafnia feedstock during plasma spraying and following cyclic oxidation, Acta Mater. 214 (2021) 117007, https://doi.org/10.1016/j.actamat.2021.117007.
[15] G. Li, X. Lu, J. Huang, S. Dong, L. Deng, J. Jiang, X. Cao, Thermal cycling behavior and failure mechanism of the Si-HfO2 environmental barrier coating bond coats prepared by atmospheric plasma spraying, J. Alloy. Compd. 913 (2022) 165319, https://doi.org/10.1016/j.jallcom.2022.165319.
[16] G. Li, J. Li, W. Chen, X. Lu, K. Lü, J. Huang, Y. Huang, L. Deng, J. Jiang, X. Cao, Cyclic oxidation and water vapor corrosion behaviors of multi-layer environmental barrier coatings with HfO2-Si bond coat for SiCf/SiC, Mater. Chem. Phys. 292 (2022) 126768, https://doi.org/10.1016/j.matchemphys.2022.126768.
[17] Q. Ding, X. Tan, L. Jiang, X. Fan, B. He, C. Wang, X. Zhuo, K. Zhou, X. Zhang, High-temperature performances of Si-HfO2-based environmental barrier coatings via atmospheric plasma spraying, Ceram. Int. 48 (16) (2022) 23127–23136, https://doi.org/10.1016/j.ceramint.2022.04.293.
[18] Z. Zhang, Y. Park, Z. Xue, S. Zhang, E. Byon, B.H. Koo, Effect of the HfO2/SiO2 premixing ratio and heating temperature on the formation of HfSiO4 as a bond coat of environmental barrier coatings, Ceram. Int. 48 (11) (2022) 15657–15667, https://doi.org/10.1016/j.ceramint.2022.02.100.
[19] W. Chen, Q. Han, J. He, W. He, W. Wang, H. Guo, Effect of HfO2 framework on steam oxidation behavior of HfO2 doped Si coating at high temperatures, Ceram. Int. 48 (14) (2022) 20201–20210, https://doi.org/10.1016/j.ceramint.2022.03.299.

[20] S. Xiao, X. Liu, Z. Chang, Y. Tian, X. Zhang, G. Han, J. Li, J. Zhang, Si-HfO2 composite powders fabricated by freeze drying for bond layer of environmental barrier coatings, Ceram. Int. 48 (13) (2022) 19266–19273, https://doi.org/10.1016/j.ceramint.2022.03.219.
[21] S. Xiao, J. Li, X. Liu, Z. Chang, P. Huang, A. Zhang, Y. Tian, X. Zhang, J. Zhang, G. Han, Exploration of the oxidation behavior and doping ratio of the Si–HfO2 bond layer used in environmental barrier coatings, Int. J. Appl. Ceram. Technol. 20 (3) (2023) 1753–1763, https://doi.org/10.1111/ijac.14319.
[22] F. Mao, Y. Niu, X. Zhong, Y. Wang, X. Zhu, L. Zhang, Q. Li, X. Zheng, Oxidation behaviors and mechanisms of Yb2O3-doped silicon coatings fabricated by vacuum plasma spray, Ceram. Int. 47 (14) (2021) 19906–19913, https://doi.org/10.1016/j.ceramint.2021.04.005.
[23] D. Fan, X. Zhong, F. Mao, Z. Zhang, R. Liang, Y. Niu, L. Wang, Q. Li, X. Zheng, High temperature performances of tri-layer environmental barrier coating with Si bond layer modified by Yb2O3, Ceram. Int. 49 (8) (2023) 11837–11845, https://doi.org/10.1016/j.ceramint.2022.12.030.
[24] H. Klemm, Silicon Nitride for High-Temperature Applications, J. Am. Ceram. Soc. 93 (6) (2010) 1501–1522, https://doi.org/10.1111/j.1551-2916.2010.03839.x.
[25] D.L. Poerschke, C.G. Levi, M. Cinibulk, Yttrium bearing silicon carbide matrices for robust ceramic composites, J. Am. Ceram. Soc. 96 (4) (2013) 1300–1308, https://doi.org/10.1111/jace.12133.
[26] Z. Sun, Y. Zhou, M. Li, Low-temperature synthesis and sintering of γ-Y2Si2O7, J. Mater. Res. 21 (6) (2006) 1443–1450, https://doi.org/10.1557/jmr.2006.0173.
[27] K. Fukuda, H. Matsubara, Anisotropic thermal expansion in yttrium silicate, J. Mater. Res. 18 (7) (2011) 1715–1722, https://doi.org/10.1557/jmr.2003.0236.
[28] C. Argirusis, T. Damjanović, G. Borchardt, Yttrium silicate coating system for oxidation protection of C/C–Si–SiC composites: Electrophoretic deposition and oxygen self-diffusion measurements, J. Eur. Ceram. Soc. 27 (2-3) (2007) 1303–1306, https://doi.org/10.1016/j.jeurceramsoc.2006.05.026.
[29] E. Courcot, F. Rebillat, F. Teyssandier, C. Louchet-Pouillerie, Thermochemical stability of the Y2O3–SiO2 system, J. Eur. Ceram. Soc. 30 (4) (2010) 905–910, https://doi.org/10.1016/j.jeurceramsoc.2009.09.007.
[30] E. García, P. Miranzo, M.I. Osendi, The prospect of Y2SiO5-based materials as protective layer in environmental barrier coatings, J. Therm. Spray. Technol. 22 (5) (2013) 680–689, https://doi.org/10.1007/s11666-013-9917-8.
[31] J.A. Thornton, The microstructure of sputter-deposited coatings, J. Vac. Sci. Technol. 4 (1986) 3059–3065, https://doi.org/10.1116/1.573628.
[32] M. Gurvitch, L. Manchanda, J.M. Gibson, Study of thermally oxidized yttrium films on silicon, Appl. Phys. Lett. 51 (12) (1987) 919–921, https://doi.org/10.1063/1.98801.
[33] T.H. Okabe, K. Hirota, E. Kasai, F. Saito, Y. Waseda, K.T. Jacob, Thermodynamic properties of oxygen in RE–O (RE=Gd, Tb, Dy, Er) solid solutions, J. Alloy. Compd. 279 (2) (1998) 184–191, https://doi.org/10.1016/S0925-8388(98)00690-2.
[34] R. Anton, N. Laska, U. Schulz, S. Obert, M. Heilmaier, Magnetron sputtered silicon coatings as oxidation protection for Mo-based alloys, Adv. Eng. Mater. 22 (7) (2020) 2000218, https://doi.org/10.1002/adem.202000218.
[35] R. Anton, S. Hüning, N. Laska, M. Weber, S. Schellert, B. Gorr, H.-J. Christ, U. Schulz, Graded PVD Mo-Si interlayer between Si coating and Mo-Si-B alloys: investigation of oxidation behaviour, Corros. Sci. 192 (2021) 109843, https://doi.org/10.1016/j.corsci.2021.109843.
[36] R. Anton, S. Hüning, N. Laska, M. Weber, S. Schellert, B. Gorr, H.-J. Christ, M. Heilmaier, U. Schulz, Interface reactions of magnetron sputtered Si-based dual layer coating systems as oxidation protection for Mo-Si-Ti alloys, Surf. Coat. Technol. 444 (2022) 128620, https://doi.org/10.1016/j.surfcoat.2022.128620.
[37] S.-K. Kang, D.-H. Ko, E.-H. Kim, M. Ho Cho, C.N. Whang, Interfacial reactions in the thin film Y2O3 on chemically oxidized Si(100) substrate systems, Thin Solid. Films 353 (1) (1999) 8–11, https://doi.org/10.1016/S0040-6090(99)00418-6.
[38] R.A. Golden, E.J. Opila, High-temperature oxidation of yttrium silicides, J. Mater. Sci. 53 (6) (2017) 3981–4000, https://doi.org/10.1007/s10853-017-1823-x.
[39] A.I. Becerro, M. Naranjo, M. Alba, J. Trillo, Structure-directing effect of phyllosilicates on the synthesis of y-Y 2 Si 2 O 7. Phase transitions in Y 2 Si 2 O 7, J. Mater. Chem. 13 (7) (2003) 1835–1842.
[40] Z. Sun, M. Li, Y. Zhou, Recent progress on synthesis, multi-scale structure, and properties of Y–Si–O oxides, Int. Mater. Rev. 59 (7) (2014) 357–383, https://doi.org/10.1179/1743280414y.0000000033.